Novak, L., *et al.*: Investigation of Vortex Shedding from an Airfoil by ...
THERMAL SCIENCE: Year 2018, Vol. 22, No. 6B, pp. 3023-3033

3023

INVESTIGATION OF VORTEX SHEDDING FROM AN AIRFOIL BY COMPUTATIONAL FLUID DYNAMIC SIMULATION AND COMPUTER-AIDED FLOW VISUALIZATION

by

Lovrenc NOVAK[*a], *Tom BAJCAR*[a], *Brane ŠIROK*[a], *Alen ORBANIĆ*[b], *and Benjamin BIZJAN*[b]

[a] Faculty of Mechanical Engineering, University of Ljubljana, Ljubljana, Slovenia
[b] Abelium d. o. o. – Research and Development, Ljubljana, Slovenia

The article presents an experimental and numerical study of vortex generation and shedding from a NACA 4421 airfoil at low Reynolds number. The experiment was conducted in a low speed wind tunnel by flow visualization. A high speed camera was used to record flow structures at the airfoil trailing edge. The recorded images were processed with an in-house developed software based on the advection-diffusion equation to compute instantaneous 2-D velocity fields. These results were compared with results of the CFD simulation which employed the scale-adaptive simulation (SAS) turbulence modelling. The SST-SAS model produced finer and less stable turbulent structures compared to an URANS simulation with the shear stress transport model. Time averaged velocities and frequency spectra for the both models are in good agreement, but variability of flow in both time and frequency domain is higher in case of the SST-SAS model. Velocity fields computed on the basis of visualization show generally acceptable agreement with the CFD results. Higher errors occur in areas of unperturbed smoke trails and areas of high velocity gradients, however, the vortex shedding frequency is captured with excellent agreement to the experiment.

Key words: *CFD, flow visualization, airfoil aerodynamics, vortex street, scale adaptive simulation*

Introduction

Knowledge on airfoil operation at low Reynolds number is important for certain applications, *i. e.* small-scale wind turbines. Under these conditions it is typical to encounter laminar separation on the airfoil suction side. At higher Reynolds numbers, flow reattaches and a laminar separation bubble is formed, whereas at lower Reynolds numbers the separated flow fails to reattach and causes formation of a wide wake. A change between the two regimes occurs over a finite range of Reynolds numbers for a given angle of attack [1]. Laminar separation has a significant effect on airfoil performance and has been a subject of many studies. However, airfoil wake characteristics at low Reynolds number are also of interest since they affect airfoil performance, impact objects downstream and can cause structural vibrations and noise. At low angles of attack it is common to encounter vortex shedding and formation of von Karman vortex street, typically when there is no reattachment of the separated layer. Most research on

---

[*] Corresponding author, e-mail: lovrenc.novak@fs.uni-lj.si

3024

Novak, L., *et al.*: Investigation of Vortex Shedding from an Airfoil by ...
THERMAL SCIENCE: Year 2018, Vol. 22, No. 6B, pp. 3023-3033

vortex shedding is focused at bluff-body wakes whereas investigations of vortex shedding in airfoil wakes are limited [2]. This paper is focused primarily on comparison of numerical and experimental methods for analysis of vortex generation and shedding from an airfoil.

Experimental approach in the present work is based on flow visualization, which enables capturing of complex time-dependant flow structures. Recorded images were analysed by a recently developed method for computer aided visualization, which enables calculation of velocity field from a series of images containing illuminated planar layer of fluid with a pollutant mixed in. The calculation method employed here is based on the advection-diffusion equation and was first introduced by Bajcar *et al.* [3]. The method is implemented into software ADM-flow, which provides all the required pre- and post-processing tools for application of the method through a graphical user interface. More information on the theoretical principles of calculation engine and verification of the method on simplified and realistic cases are given in Bizjan *et al.* [4, 5].

In addition to the experiment, numerical (CFD) calculations were performed to calculate and visualize flow around the airfoil. Key issue for most applications of CFD, including flows around airfoils, is modelling of turbulence. In cases where detailed information on turbulent structures is required such as massively separated flows, turbulence has to be resolved by using methods such as large eddy simulation (LES) or hybrid RANS-LES methods, such as detached eddy simulation (DES) [6]. Another recent hybrid model is the scale-adaptive simulation (SAS), which in many ways behaves similar to the DES. The SAS model was developed by Menter and Egorov [7] and is in fact an improved URANS model, with LES capability in unstable flow regions. It offers a single framework which covers both steady state RANS and LES regions without an explicit switch in the model formulation, such as the grid limiter in DES. The SAS model is based on introduction of the von Karman length scale into the turbulent length scale equation of a two-equation turbulence model. This provides means for local detection of unsteadiness and automatic balancing between contributions of modelled and resolved turbulence stresses. The SAS concept was initially developed for the k-$k^{1/2}L$ turbulence model [8] and then extended to the SST model [7].

Reported applications of the SAS model for calculation of flow around airfoils are very rare compared to the DES or LES based calculations. Its application is reported in some turbomachinery applications such as fans [9] or hydraulic machinery [10-12], where it showed prediction capabilities comparable to LES. Derakhshandeh *et al*. [13] analysed unsteady flow around two circular cylinders and showed that predictions from the SAS model were more accurate compared to the SST model. Assessment of the SAS and other turbulence models for the simulation of turbulent flows past bluff bodies was done by Elkhoury [14]. In aerodynamics, comparisons of DES and LES with the direct numerical simulation (DNS) and experiments generally show improved predictions compared to RANS, but especially with LES, computational requirements are still limiting for a more widespread use. The SAS offers a good alternative to DES especially with its flexibility and robustness in regard to the grid density and chosen time step.
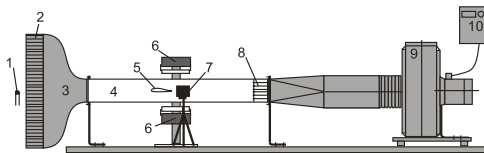
Figure 1. Experimental station; *1 – smoke generation wire, 2 – flow straightener, 3 – contraction section, 4 – test section, 5 – air foil, 6 – LED lighting, 7 – high speed camera, 8 – flow straightener, 9 – radial fan, 10 – frequency inverter*

Experimental set-up

Measurements with flow visualization were performed in a low-speed wind tunnel as shown on fig. 1. The test section of the tunnel

Novak, L., *et al.*: Investigation of Vortex Shedding from an Airfoil by ...
THERMAL SCIENCE: Year 2018, Vol. 22, No. 6B, pp. 3023-3033

3025

has a square 100×100 mm cross-section and is 800 mm long. Upstream of the test section a contraction section with an inlet size of 400×400 mm is installed. A honeycomb structure at the wind tunnel inlet and downstream the test section is used to straighten the flow and assure stationary vortex-free flow field in the test section area. A HF R ϕ140-17D radial fan was connected to the test section outlet by a flexible pipe. A frequency inverter regulation was used to set fan rotational speed and achieve the required air velocities in the tunnel.

A NACA 4421 airfoil with a chord length of 30 mm was used as the test object. The airfoil type and size were chosen in relation to a previous experiment, dealing with axial fan hollow blades [15]. The airfoil was mounted horizontally in the middle of the test section, spanning the entire width of the test section. The angle of attack could be adjusted by manual rotation and tightening of the back end-plate. All experiments were performed with the airfoil at 3° angle of attack, which ensured flow separation and vortex shedding to occur on the airfoil suction side, while the boundary-layer on the airfoil pressure side remained stable.

Velocity profile 50 mm upstream of the airfoil leading edge was determined by using hot-wire anemometry. Measurements were taken at 18 equally spaced points aligned on a vertical line at midspan position. Measuring equipment and procedures are described in more detail in [15]. The measured velocity distribution and turbulence intensity could be later applied as a boundary condition for the CFD calculations.

Experimental flow visualization was achieved by introducing passive tracer smoke into fully developed flow. Smoke was generated by vaporizing paraffin oil on a heated coil, made of a thin stainless steel wire. The coil was positioned at the wind tunnel inlet, just outside the honeycomb structure. A Fastec HiSpec4 2G Mono high speed camera was used to record visualized flow. The camera was placed perpendicular to the wind tunnel. Recording frequency was 8103 frames per second using 121 μs exposure time and 50 mm lens were used with the aperture setting of f/2. Recorded images had 8-bit grey level depth and resolution of 752×224 pixels, where pixel size was calculated as $p = 0.09$ mm. Due to the short exposure time, a powerful source of illumination was needed. For that purpose two LED lights were used, one of them placed above and one below the airfoil. For each measurement, a sequence of 2000 images was recorded. The number of images was limited by the time of uniform passive tracer smoke generation. Recorded images were processed in ADM-flow software to calculate velocity fields. Physical parameters in ADM-flow were set to match the actual camera recording speed and pixel size. Diffusion coefficient was set to 10^{-7} m²/s. Its variation showed no significant influence on calculated velocity fields, which indicates the advection dominated nature of the investigated flow. Effects of other settings in ADM-flow were analysed in detail in [4, 5], where accuracy of the method was also evaluated on the basis of synthetic images. Analysis of vortex shedding in [4] resulted in global relative errors of up to 14% in vector magnitude and 15° in direction for the most difficult flow pattern (vortex). In the present case, additional uncertainties are introduced from the experiment, where camera capabilities, especially frame rate, could prove to be important. However, the frame rate was kept at maximum possible level and its effect on uncertainty was currently not analysed.

Numerical set-up

Geometry of the numerical model was made to represent the actual wind tunnel where the experiments were conducted. Numerical simulations were performed for the airfoil at 3° angle of attack. The computational domain covers the entire height of the wind tunnel (100 mm) in direction normal to the airfoil (y co-ordinate) and has a length of 200 mm in the stream-wise direction (x co-ordinate) with the airfoil leading edge at $x = 50$ mm. A C-type grid with 473 cells
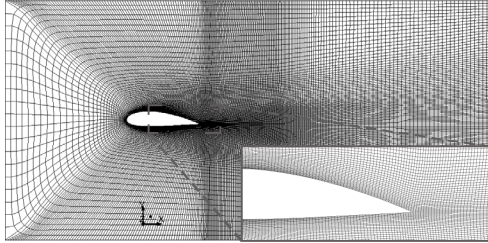
Figure 2. Computational grid

in wall parallel direction (177 of those bordering the airfoil) and 62 cells in wall normal direction was generated in the *x-y* plane of the domain, fig. 2. This grid was extruded in the span-wise direction with 37 cells of constant width, totalling to 50% chord length or 15% of the actual tunnel and airfoil width. The grid consists of a total of 1085062 hexa cells.

Variable grid spacing is used in both directions of the C grid with focus on proper resolution of the airfoil boundary-layer and wake region. Initial cell height on the airfoil was set to produce values of $y^+ < 1.6$. Grid in the wake region up to 1 chord downstream of the trailing edge is designed to give highly orthogonal and low aspect ratio cells since this is the main area of interest for the simulation. Further downstream the grid is gradually stretched in stream-wise direction.

Top and bottom of the domain are defined as no slip walls, since they represent the actual wind tunnel walls. Periodic boundary conditions are imposed on the span-wise boundaries. Inlet velocity profile is set according to the measured data, obtained with the hot-wire anemometry at 18 equally spaced locations across the channel height. The average inlet velocity is 4.94 m/s. Turbulence intensity of 1.5% was computed from the hot-wire measurements and set as inlet turbulence, while the inlet turbulent length scale of 5 mm was estimated based on the upstream flow straightener geometry. Outlet is defined as a pressure outlet with constant relative pressure of 0 Pa.
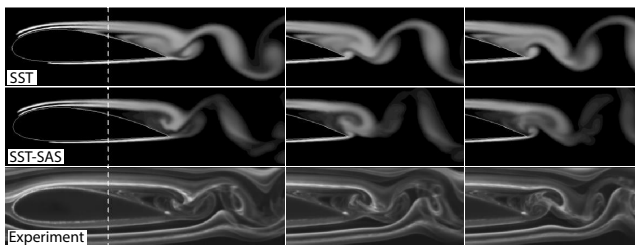

Figure 3. Sequence (1 ms time between images) of instantaneous volume fractions of secondary fluid (smoke) for the SST and the SST-SAS model compared to the experimental visualization

To visualize the numerically predicted flow patterns in a similar way to the real experimental visualization a secondary fluid, acting as a pollutant, was introduced in the numerical model. The secondary fluid was injected at three different locations in the boundary-layer close to the airfoil leading edge, fig. 3. Both primary and secondary fluids were defined with identical properties (air at constant density and viscosity). The mixture multi-phase model was used to calculate the flow of both phases. Since the relative velocity between the phases was set to zero a homogeneous multi-phase flow was simulated. Injections of the secondary phase were done by using source terms in individual cells. Each injection cell was set-up with a mass source of secondary phase and an equally potent mass sink of primary phase to ensure continuity of flow. Injection mass rates were set through a user defined function (UDF) as s sum of a constant and a random part at a ratio of 3:1. The random part was updated each time step to produce a time-varying injection rate, which enabled better flow visualization.

Time step for the simulation was chosen with respect to the computed local Courant-Freiedrichs-Lewy (CFL) numbers and to the frame rate of the high speed camera (8103 fps) that was used in the experiment. Calculations at a time step of $4.1137 \cdot 10^{-5}$ seconds, which equals one third of the camera's time per frame, produced CFL numbers in the wake area

Novak, L., *et al.*: Investigation of Vortex Shedding from an Airfoil by ...
THERMAL SCIENCE: Year 2018, Vol. 22, No. 6B, pp. 3023-3033

3027

ranging between 0.3 and 1.8, with average slightly below the recommended value of unity. By saving images from every third time step the numerical visualization frame per second could be matched with the experimental frame per second.

Both the SST model in unsteady mode and the SST-SAS model were used for the simulations. The SST model is a two-equation eddy viscosity turbulence model with improved prediction of separation compared to earlier models such as the k-ω model, and is one of the most successful RANS models for aerodynamics simulations with separation [16], even in the most complex cases such as turbomachinery flows in rotating environments [17]. The SST-SAS represents an upgrade of the SST model, as explained earlier in the introduction chapter. Initial conditions for the simulations were always provided by the steady-state solution using the SST model. Both models were used with the default coefficients as set in ANSYS FLUENT 13.0 [18]. The SST model was run with the low-Reynolds number corrections enabled. These corrections damp the turbulent viscosity and can affect the laminar-turbulent transition process by producing a delayed onset of the turbulent wall boundary-layer. In other words, they constitute a very simple model for laminar-turbulent transition [18]. Effects of enabling the low-Reynolds number corrections were not quantitatively assessed in the present study, but it was estimated that they contribute to a slightly better resolution of flow in the separated region.

The segregated solver and the SIMPLE scheme for the pressure-velocity coupling were employed for all the calculations. Spatial discretization methods were generally second order schemes with the exception of the phase volume fraction equation, where the QUICK scheme was used, and the momentum equation for the SST-SAS model, where the bounded central differencing scheme was used following the recommendations in [18].

All calculations were performed on a high performance computer using 24 CPU. Five to six iterations per time step were required to reach a 10^{-3} absolute residual for the volume fraction equation and a $5 \cdot 10^{-4}$ absolute residual for the continuity equation. The momentum and turbulence related absolute residuals typically dropped two orders of magnitude per time step to values well below 10^{-4}. Excellent convergence in time was achieved with periodicity in residual values and main flow variables.

Results

In all the simulations, the Reynolds number based on the chord length is $Re_c = 10^4$. In both SST and SST-SAS computed cases, flow separates at around 39% of the chord length on the suction side and stays attached on the pressure side. The flow separation location is independent of time. The separated shear layer on the suction side becomes unstable, starts to oscillate and finally rolls-up into large-scale vortices, which are periodically shed downstream.

Flow visualization images resulting from the numerical simulation and the experiment at approximately the same vortex shedding phases are shown on fig. 3. Numerical results are presented on a plane of constant span-wise co-ordinate, which is set to cut through the middle of the secondary fluid injection cells. The images are produced by plotting contours of volume fraction of secondary fluid in a black-white scale. Both the SST and the SST-SAS simulations enabled visualization of vortex shedding patterns with reasonable detail. Slightly more homogenous distribution of secondary fluid concentration can be seen in case of the SST model. Also, higher penetration of secondary fluid from the vortex generation area at the trailing edge to the upstream area of reversed flow is visible for the SST model. This is partly due to less span-wise mixing predicted in case of the SST model. Visualization with the SST-SAS model resulted in similar flow patterns but with slightly more detail and finer structures visible

3028

Novak, L., *et al*.: Investigation of Vortex Shedding from an Airfoil by ...
THERMAL SCIENCE: Year 2018, Vol. 22, No. 6B, pp. 3023-3033

in the vortex generation region at the airfoil trailing edge. Dissipation of secondary fluid further downstream is higher in case of the SST-SAS model, which is again linked to higher span-wise velocities and more intense mixing.

Comparison of numerical and experimental visualization images on fig. 3 is limited to three different states, separated by a time interval of 1 ms. Examination of subsequent images, which are not presented here due to space constraints, shows that the patterns repeat periodically with only slight differences, caused by the randomness in smoke injection intensity. Nevertheless, visual comparison of numerical and experimental image sequences shows very similar patterns, with better agreement in case of the SST-SAS model. Slight differences are notable at vortex generation and shedding location in stream-wise direction, where numerical calculations appear to predict these locations slightly upstream to the actual visualized flow. Visible detail is generally better in the experiment, where thinner and more numerous smoke trails were generated.

Velocity field in the trailing edge region, where vortex generation and shedding takes place, is presented in more detail on fig. 4. The length of the shown velocity vectors is not scaled with the velocity magnitude in order to better present the flow patterns. Results of the CFD simulations are compared to the results of computer aided visualization (CAV) analysis
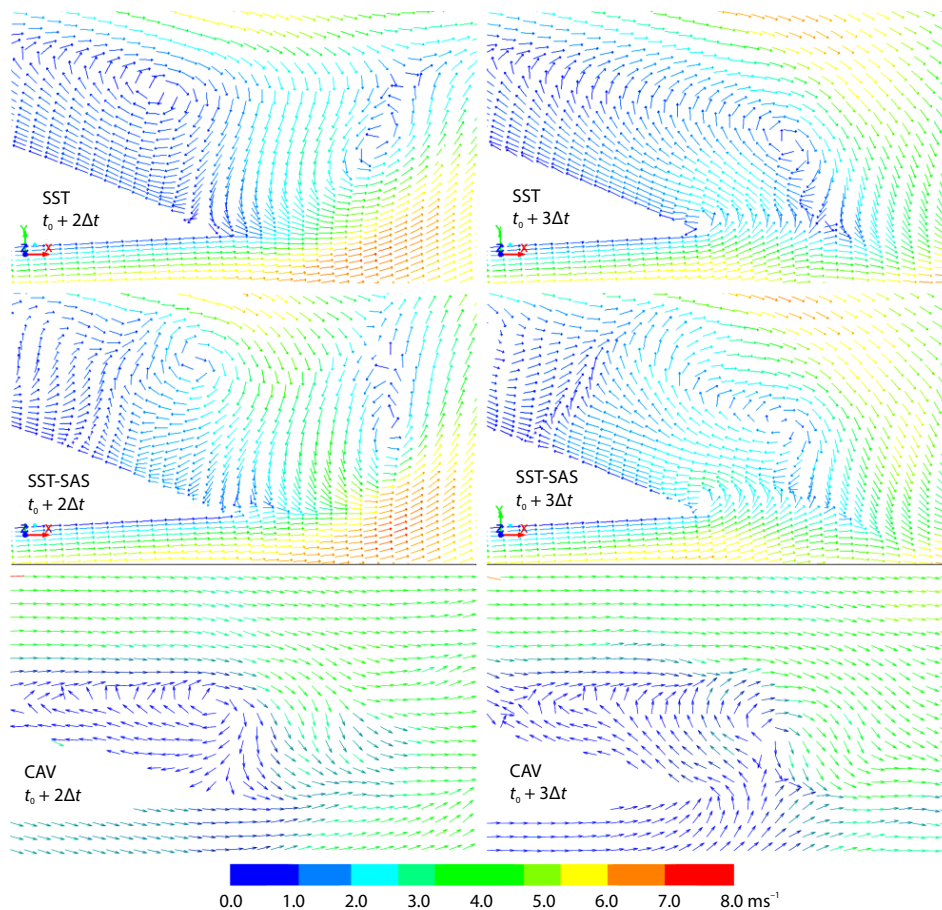

Figure 4. Sequence of computed velocity fields for the SST model, the SST-SAS model, and the CAV method at time interval of $\Delta t = 1.24$ ms (*for color image see journal web site*)

Novak, L., *et al.*: Investigation of Vortex Shedding from an Airfoil by ...
THERMAL SCIENCE: Year 2018, Vol. 22, No. 6B, pp. 3023-3033

3029

with the ADM-flow code. Each displayed CAV vector represents an average velocity vector calculated from the underlying square of 5×5 pixel size. The CFD predicted velocity fields clearly show the mechanism of periodic vortex generation and shedding. Conditions are in many ways similar to the well investigated case of vortex shedding behind cylinders [19], but with significant differences due to the specific, non-symmetric geometry. A vortex with clockwise rotation is generated at the interface of the separated layer and re-circulating flow above the airfoil suction side. A vortex with counter-clockwise rotation is generated at the airfoil trailing edge. Both vortices are generated alternately. In the generation (growing) phase the centres of both vortices move downstream and start to accelerate more rapidly once they reach the trailing edge, where they are shed to form the von Karman vortex street.

Calculations with the SST model predict very stable periodic flow conditions, with a simpler and more organized vortex patterns compared to the SST-SAS model calculations, where instability is most evident in the re-circulating boundary-layer. Instability is best reflected in instable inception location of the clockwise (upper) vortex as well as in variation of its intensity and shape as it moves downstream. The SST-SAS also gives a highly 3-D, non-homogenous and unsteady velocity field in the region of re-circulating flow above the airfoil suction side. Generation and dissipation of smaller vortices can be detected in this region. None of these develops in case of the SST model, where flow above the suction side is steady and uniformly directed reverse to the main flow.

Velocity fields calculated by the CAV method follow similar patterns to the CFD results. Most evident differences occur at the lower part of observed window, with flow velocities at the airfoil pressure side significantly under-predicted. Also, resolution of vertical structures by the CAV method is not always successful. Another notable difference is in the extent of the re-circulating flow above the airfoil suction side, where CAV shows a lower re-circulating region. Many deficiencies in the CAV results could stem from the actual input images not carrying enough information (greyness gradients) for the algorithm to be able to calculate proper velocities. This situation is especially evident in larger black regions (no smoke) or in regions of unperturbed smoke trails, such as upstream the airfoil or in the attached boundary-layers. Another reason for lost detail is related to the fact that the studied flow is complex and highly unsteady and since the CAV method utilizes some temporal and spatial smoothing it is inevitable to introduce a certain amount of averaging in the results.

Further comparison of calculated velocities for the SST, SST-SAS, and CAV cases is presented on fig. 5. Velocity profiles are plotted for three vertical sample lines, where line 1 is located at the trailing edge, line 0 is one third chord length upstream and line 2 one third chord length downstream of line 1, fig. 5. Thick lines on charts represent time-averaged values for approximately 39 vortex shedding periods long data series whereas thin lines represent the 10th and 90th percentile of values for a given co-ordinate.

At line 0, both numerical models are in excellent agreement, with the conditions being almost steady-state. Slight differences and time-varying conditions can be detected only at the span-wise velocity component. The CAV method had difficulties in calculating velocities at line 0 due to the very steep stream-wise velocity gradient between the creeping reversed flow and an order of magnitude faster main flow. At line 1 and line 2 the velocity field is time-dependant in all three directions. Numerical calculations by both turbulence models result in a good agreement between the time-averaged values, however, the predicted velocity fluctuations are generally larger in case of the SST-SAS model. Significant differences can be seen in the predicted span-wise velocities, where the SST model shows almost steady-state conditions, whereas the SST-SAS calculations clearly predict a time-variable span-wise component. As expected, the
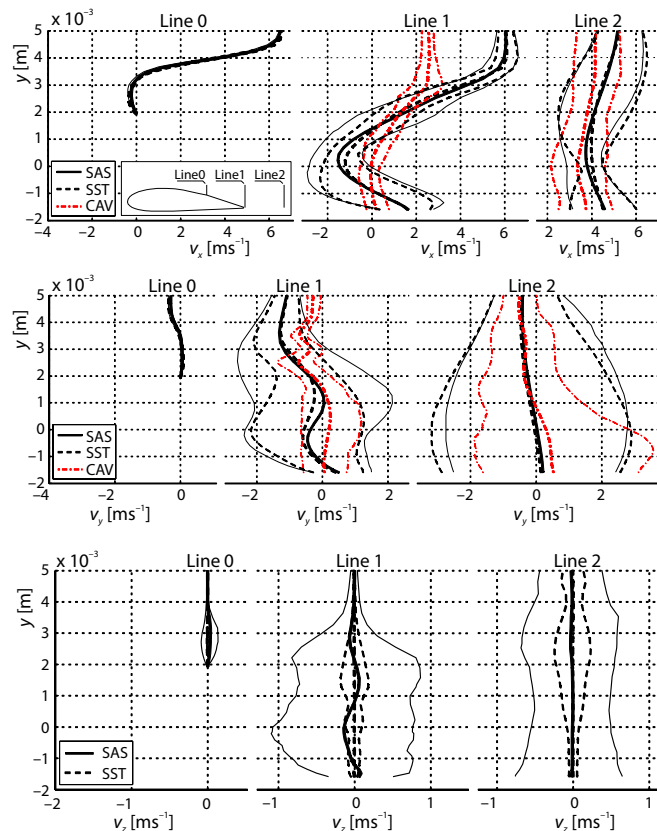
Figure 5. Streamwise (v_x), vertical (v_y), and spanwise (v_z) velocity components at three vertical sample lines; thick curves represent time averaged values, thin curves represent the 10th and the 90th percentile of data for 39 vortex shedding periods

isotropic turbulence modelling by the SST model is not capable of capturing the relatively small flow instabilities in span-wise direction. On the contrary, a fully 3-D transient velocity field develops in case of the SST-SAS model, where sufficiently small turbulent structures are actually resolved.

Results by the CAV method at line 1 are taken from the same series of calculations as presented on fig. 4. For line 2, a separate square window with 20×100 pixel size was analysed by the CAV. Better agreement between the CAV and the numerical time-averaged profiles is reached at line 2. At line 1, highest differences exist in its upper part, where CAV calculated velocities are significantly smaller compared to the numerical ones. This is most probably a consequence of insufficient perturbations in smoke concentration in this region. Generally, the 10th and 90th percentile curves for the CAV results indicate less temporal variation in velocity values compared to the numerical results. This could be attributed to the method's inherent time-averaging. Another influence to be considered in relation to the CAV method is the presence of flow in the third dimension, which the method cannot resolve. Spanwise smoke transport means alteration of smoke distance from the camera (depth) and is actually captured in the images; however its effects on the method uncertainty are currently impossible to assess. Based on comparison between SST and SAS results, which could be interpreted as comparison

Novak, L., *et al.*: Investigation of Vortex Shedding from an Airfoil by ...
THERMAL SCIENCE: Year 2018, Vol. 22, No. 6B, pp. 3023-3033

3031

between 2-D and 3-D flow, we estimate that treatment of flow as either 2-D or 3-D introduces errors that are minor compared to the total errors that exist between the CFD and CAV results.

Final comparisons of the CFD, CAV, and experimental results are presented by carrying out frequency analysis on sampled data at line 0, line 1, and line 2. Time series for each line were created as sequences of average values of each velocity component and greyness level along the line. In case of the CFD simulations the time series consisted of 4096 values and in cases of the experimental visualization and CAV they contain one third of that due to the sampling rate being three times lower. Fast fourier transform algorithm was used on all the time series to generate the power spectra presented on figs. 6 and 7. The stream-wise velocity spectra are not presented here since they generally contain the same peaks as the corresponding vertical velocity spectra, but with smaller amplitudes. The vertical velocity spectra at line 2, fig. 6(b), show prominent peaks for both the numerical and the CAV results. The first peak, occurring at around 280 Hz for the SST and SST-SAS calculations, corresponds to the vortex shedding frequency. In case of the SST model the spectra are very smooth compared to the SST-SAS results which reflect higher scatter of frequencies in the data. Similar observations can be made for the span-wise velocity spectra at line 2, fig. 7(a), where a clear peak is detectable at 140 Hz (sub-harmonic of the vortex shedding frequency) for the SST model, whereas a more random distribution with no dominant peaks is seen in case of the
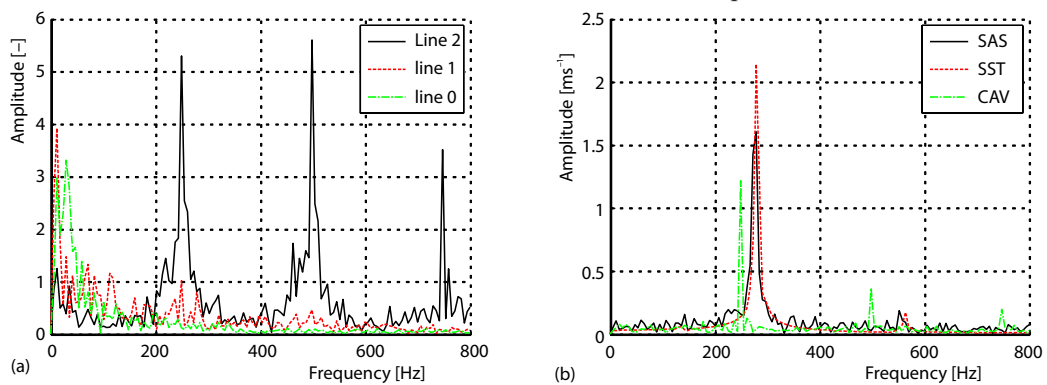
Figure 6. Frequency spectra of (a) experimentally obtained average greyness level along line 0, line 1, and line 2, and (b) computed average vertical velocity along line 2 for different models (*for color image see journal web site*)
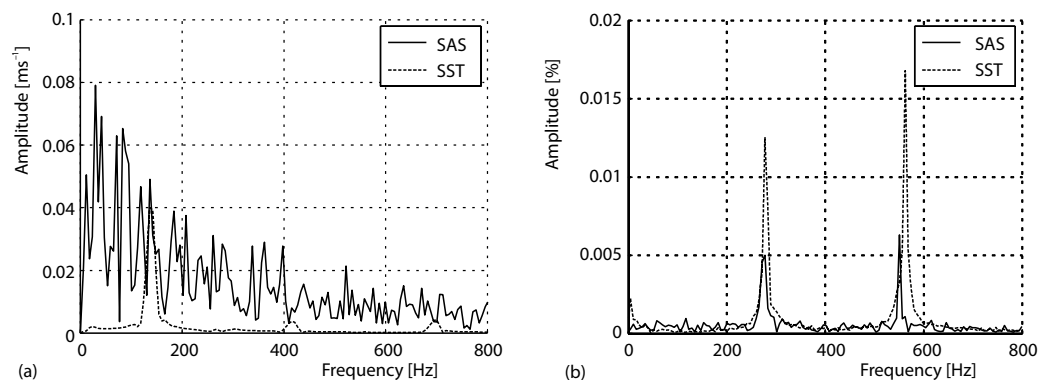
Figure 7. Frequency spectra of numerically obtained averaged values along line 2; (a) span-wise velocity and (b) secondary fluid volume fraction (*for color image see journal web site*)

3032

Novak, L., *et al*.: Investigation of Vortex Shedding from an Airfoil by ...
THERMAL SCIENCE: Year 2018, Vol. 22, No. 6B, pp. 3023-3033

SST-SAS model. Secondary fluid volume fraction (greyness level) spectra for both numerical cases at line 2, fig. 7(b), shows distributions similar to those from the vertical velocity spectra, fig. 6(b). A significant difference is the strength of the second harmonic, which surpasses the strength of the fundamental frequency. More important, a shift between the SST and the SST-SAS second harmonic peak frequency can be seen. The SST peak occurs at 564 Hz and the SST-SAS peak at 552 Hz, indicating the actual vortex shedding frequency to be around 282 Hz and 276 Hz, respectively.

Frequency analysis of experimental visualization data (greyness levels) and CAV results (vertical velocity) are presented in fig. 6. The experimental greyness spectrum at line 2, fig. 6(a), has strong peaks at 250 Hz, 500 Hz, and 750 Hz, corresponding to the fundamental vortex shedding frequency and its harmonics. At line 0 and line 1 the vortex shedding frequency peaks are visible but appear insignificant. The spectrum of CAV vertical velocity at line 2, fig. 6(b) has peaks at exactly the same frequencies than the experimental greyness level at line 2. This means that the CAV method was time-accurate at capturing dynamic properties of the observed fluid flow.

The most significant differences between the experimental/CAV and numerical SST/SST-SAS spectra are the fundamental and consequently harmonic frequency values. Both numerical models predict fundamental frequency at around 280 Hz, which is an overprediction of 12% compared to the experimental data. Judging from the second harmonic, the SST-SAS model actually predicts 276 Hz while the SST predicts 284 Hz, making the SST-SAS result slightly more accurate than the SST result.

Conclusions

Numerical simulations with both the SST and the SST-SAS models predicted periodic shedding of large scale vortices and formation of flow patterns, consistent with the experimentally observed flow. The numerical calculations indicate more structured flow patterns and higher mixing of fluids in case of the SST-SAS model, compared to the SST model. Investigation of velocity fields showed increased complexity, three-dimensionality and non-homogeneity predicted by the SST-SAS model, with a higher degree of velocity fluctuations present. The SST model produced a highly periodic and stable flow, whereas the SST-SAS model predicted slight instabilities in the recirculating boundary-layer, which resulted in non-periodic inception location, intensity, and shape of the clockwise (upper) vortex. The increased complexity of turbulent flow produced by the SST-SAS model also reflects in the frequency domain, with spectra showing a wider range of contained frequencies compared to the SST model. The fundamental vortex shedding frequency predicted by the numerical simulations is around 12% higher than the frequency, calculated from experimental data.

The CAV method produced velocity fields similar to the CFD predicted flow. Most notable differences between the CAV and the CFD velocity fields could be seen in the extent of re-circulating flow above the airfoil suction side and in the resolution of large scale vortices, where the CAV method performed inconsistently. Reasons for decreased accuracy of the CAV method could partly be related to its sensitivity to the quality of input images, which should ideally contain sufficient greyness gradients across the whole area of interest. Another major reason affecting the CAV performance could be attributed to the fact that the studied flow was complex and highly unsteady, which probably led to higher errors due to the temporal averaging and spatial smoothing, inherent to the method. However, the dynamics of the flow in terms of vortex shedding frequency was captured by the CAV method with excellent agreement to the experiment.

Nomenclature

c — chord length, [m]
k — turbulent kinetic energy, [m²s⁻²]
L — length scale, [m]
Re_c — Reynolds number based on chord length, $(=Uc/\nu)$
t — time, [s]
u_τ — friction velocity, [–]
U — free-stream velocity, [ms⁻¹]
y — distance from the wall, [m]
y^+ — non-dimensional wall distance, $(=u_\tau y/\nu)$

Greek symbols

ε — turbulent dissipation rate, [m²s⁻³]
ν — kinematic viscosity, [m²s⁻¹]

Acronyms

CAV — computer aided visualization
CFL — Courant-Friedrichs-Lewy
DES — detached eddy simulation
DNS — direct numerical simulation
LES — large eddy simulation
SAS — scale adaptive simulations
UDF — user defined function

References

[1] Carmichael, B. H., *Low Reynolds Number Airfoil Survey*, NASA Washington DC, CR 165803, Vol. 1, 1981
[2] Yarusevych, S., *et al.*, On Vortex Shedding from an Airfoil in Low-Reynolds-Number Flows, *Journal Fluid. Mech.*, *632* (2009), Aug, pp. 245-271
[3] Bajcar, T., *et al.*, Quantification of Flow Kinematics Using Computer-Aided Visualization, *Strojniški vestnik – Journal of Mechanical Engineering, 55* (2009), 4, pp. 215-223
[4] Bizjan, B., *et al.*, Flow Image Velocimetry Method Based on Advection-Diffusion Equation, *Strojniški vestnik – Journal of Mechanical Engineering, 60* (2014), 7-8, pp. 483-494
[5] Bizjan, B., *et al.*, A Computer-Aided Visualization Method for Flow Analysis, *Flow Measurement and Instrumentation*, *38* (2014), Aug., pp. 1-8
[6] Spalart, P. R., *et al.*, Comments on the Feasibility of LES for Wings and on the Hybrid RANS/LES Approach, *Proceedings*, 1ˢᵗ AFOSR International Conference on DNS/LES, Columbus, La., USA, 1997, pp. 137-147
[7] Menter, F. R., Egorov, Y., The Scale-Adaptive Simulation Method for Unsteady Turbulent Flow Predictions – Part 1: Theory and Model Description, *Flow Turbulence Combustion, 85* (2010), 1, pp. 113-138
[8] Menter, F. R., *et al.*, Steady and Unsteady Flow Modelling Using the k-$k^{1/2}L$ model, *Proceedings*, The Int. Symp. on Turbulence, Heat and Mass Transfer, Dubrovnik, Croatia, 2006, Vol. 5, pp. 403-406
[9] Younsi, M., *et al.,* Application of the SAS Turbulence Model to Predict the Unsteady Flow Field Behaviour in a Forward Centrifugal Fan, *Int. J. of Computational Fluid Dynamics, 22* (2008), 9, pp. 639-648
[10] Lucius, A., Brenner, G., Unsteady CFD Simulations of a Pump in Part Load Conditions Using Scale-Adaptive Simulation, *Int. J. of Heat and Fluid Flow, 31* (2010), 6, pp. 1113-1118
[11] Škerlavaj, A., *et al.,* Choice of a Turbulence Model for Pump Intakes, *Proceedings of the Institution of Mech. Engineers, Part A*: *Journal of Power and Energy*, *225* (2011), May, pp. 764-778
[12] Jost, D., *et al.*, Improvement of Efficiency Prediction for a Kaplan Turbine with Advanced Turbulence Models, *Strojniški vestnik – Journal of Mech. Engineering*, *60* (2014), 2, pp. 124-134
[13] Derakhshandeh, J. F., *et al.*, The Effect of Arrangement of Two Circular Cylinders on the Maximum Efficiency of Vortex-Induced Vibration Power Using a Scale-Adaptive Simulation Model, *Journal of Fluids and Structures, 49* (2014), Aug., pp. 654-666
[14] Elkhoury, M., Assessment of Turbulence Models for the Simulation of Turbulent Flows Past Bluff Bodies, *Journal of Wind Engineering and Industrial Aerodynamics*, *154* (2016), July, pp. 10-20
[15] Eberlinc, M., *et al.*, Experimental Investigation of the Interaction of Two Flows on the Axial Fan Hollow Blades by Flow Visualization and Hot-Wire Anemometry, *Experimental Thermal and Fluid Science, 33* (2009), 5, pp. 929-937
[16] Leschziner, M. A., Modelling Turbulent Separated Flow in the Context of Aerodynamic Applications, *Fluid Dynamics Research, 38* (2006), 2-3, pp. 175-210
[17] Sekavčnik, M., *et al.*, Heat Transfer Evaluation Method in Complex Rotating Environments Employing IR Thermography and CFD, *Experimental Heat Transfer, 21* (2008), 2, pp. 155-168
[18] ***, ANSYS Inc., ANSYS Fluent Release 13.0 User's Guide, 2010
[19] Berger, E., Wille, R., Periodic Flow Phenomena, *Annual Reviews of Fluid Mechanics*, *4* (1972), Jan., pp. 313-340